Fast Calculation of Electromagnetic Forces in IPMSMs Under PWM VSI Supply Based on Small-Signal Time-Harmonic Finite Element Method

Sa Zhu, *Member, IEEE*, Jianbo Lu, and Feng Zeng

***Abstract*—This paper introduces a novel method for fast calculating the electromagnetic forces in interior permanent magnet synchronous machines (IPMSMs) under pulse width modulation (PWM) voltage source inverter (VSI) supply based on the small-signal time-harmonic finite element analysis (THFEA), which has been successfully utilized for fast calculating the PWM-induced losses in silicon steel sheets and permanent magnets. Based on the small-signal THFEA, the functional relationships between high-frequency harmonic voltages (HFHVs) and corresponding airgap flux densities are established, which are used for calculating the flux density spectra caused by each HFHV in the PWM voltage spectra. Then, the superposition principle is applied for calculating the flux density spectra caused by fundamental currents and all HFHVs, which are converted to the electromagnetic force spectra at last. The relative errors between the force density spectra calculated with the proposed method and those obtained from traditional time-stepping finite element analysis (TSFEA) using PWM voltages as input are within 3.1%, while the proposed method is 24 times faster than the traditional TSFEA.**

***Index Terms*—Time-harmonic finite element analysis (THFEA), Interior permanent magnet synchronous machines (IPMSMs), Electromagnetic forces, Pulse width modulation, Vibration and acoustic noise.**

I. INTRODUCTION

INTERIOR permanent magnet synchronous machines (IPMSMs) are widely applied in electrical vehicles and industries in modern times [1]. The accurate modeling of the electromagnetic noise and vibration characteristics of IPMSMs is essential for their optimal design, which requires accurate electromagnetic force calculations on the inner surfaces of stators [2]-[10]. Because of the nonlinearity of IPMSMs, finite element analysis (FEA) is the most widely used methods for the accurate force calculation, which is however time-consuming [2]-[6]. Especially, when the pulse width modulation (PWM) effects are considered, fine steps are needed to distinguish high-frequency components if the traditional time-stepping FEA (TSFEA) is used, disregarding current sources contained high-frequency harmonic currents (HFHCs) or PWM voltages are used as the input for the transient calculation [7]-[11]. Numerous researches have been conducted on the influence of control and modulation strategies on electromagnetic forces and consequent vibrations and noises [12]-[16]. However, these investigations are mainly based on experiments, which have not addressed a fast and accurate method for calculating high-frequency electromagnetic forces caused by different PWM-induced high-frequency harmonic voltages (HFHVs).

Neglecting the nonlinearity of silicon steel sheets (SSTs), a method for fast calculating electromagnetic forces caused by HFHCs has been proposed in [17] based on the superposition principle, which uses the permeance distribution function to describe the relationships between input currents and flux density distributions. However, the HFHCs themselves are very difficult to be accurately predicted at the design stage because of the eddy current reaction effects at high frequency under PWM voltage source inverter (VSI) supply [11]. Besides, the superposition principle and other analytical methods [17]-[20] can only be applied under the assumption of neglecting the nonlinearity of SSTs, which is not fit for IPMSMs. To tackle the nonlinearity in IPMSMs, the small-signal time-harmonic FEA (THFEA) based on the frozen differential reluctivity tensor method (FDRTM) has been proposed for fast calculating the PWM-induced permanent magnet (PM) eddy current losses and iron losses [21]-[23]. In this paper, the small-signal THFEA method is further extended for calculating the airgap flux densities and electromagnetic forces caused by HFHVs.

This paper focuses on presenting a detailed procedure for fast calculating the electromagnetic forces in IPMSMs under PWM VSI supply. Although only the calculation procedure at one working condition is given and the eddy current reaction effect in PMs is neglected, the proposed method is able to consider different working conditions and the eddy current reaction effect, just like the calculation of the PWM-induced losses in [21]-[23], with more THFEA and interpolation methods, which is no longer repeated here. Fig. 1 gives an overview of the proposed fast calculation method. In Section II-*A*, a new computational efficient FEA (CE-FEA) method based on the *dq* transformation is proposed for fast calculating airgap flux density under sinusoidal current source (SCS) supply, which has similar effects with the CE-FEA method in [24] but

Manuscript received January 28, 2022; revised February 19, 2022; accepted February 28, 2022. date of publication March 25, 2022; date of current version March 18, 2022.

This work was supported in part by the National Natural Science Foundation of China under projects 51907053, by Natural Science Foundation of Jiangsu Province of China under Project BK20190489, by the Fundamental Research Funds for the Central Universities under grant B200202167, and by the China Postdoctoral Science Foundation under grant no. 2019M661708.

Sa Zhu, Jianbo Lu, and Feng Zeng are with the College of Energy and Electrical Engineering, Hohai University, Nanjing, 211100, China (e-mail: zhusa@hhu.edu.cn).

(Corresponding author: Sa Zhu).

Digital Object Identifier 10.30941/CESTEMS.2022.00010

2096-3564 © 2022 CES

different ways. In Section II-*B*, the flux densities under one pole generated by independent *d*- and *q*-axis HFHV excitations are calculated, respectively, which establishes the functional relationships between HFHVs and corresponding flux densities. In Section II-*C*, for a simple introduction, the flux density spectra generated by one positive rotational HFHV are calculated based on the functional relationships, which is verified with the TSFEA method. In Section II-*D*, the flux density spectra caused by all the PWM-induced HFHVs are calculated and verified. In Section III, the analytical method used for converting flux density spectra to force density spectra is introduced. In Section IV, conclusions are made, which demonstrates the calculation speed of PWM-induced forces is improved by 24 times, while relative errors between the proposed method and TSFEA are within 3.1%.

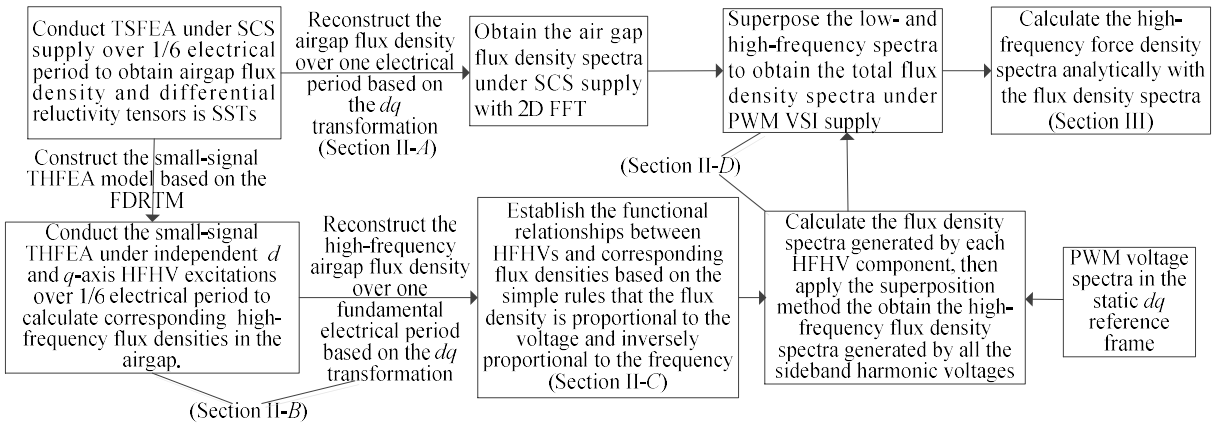

Fig. 1. Flowchart of the proposed method for fast calculating PWM-induced electromagnetic forces

II. Calculation of High-Frequency Flux Density Spectra at One Working Condition

The IPMSM reported at [11] is taken as the prototype machine for the calculation, which has 3 pole pairs, 36 slots, and distributed windings. The skewed-slots effect is neglected for simplicity in this paper. One working condition shown in Table I is analyzed in this Section to illustrate the detailed procedure of the proposed method. The fundamental frequency f_o is 50 Hz according to the parameters in Table I.

Table I
The Working Condition Analyzed in Section II

Speed n	D-axis current i_d	Q-axis current i_q
1000 r/min	0	$13\sqrt{2}A$
PWM strategy	DC-bus voltage U_{dc}	Carrier frequency f_c
Space vector PWM	554 V	4 kHz

A. Fast Calculation of Airgap Flux Density Under SCS Supply Based on DQ Transformation

The common practice to calculate the radial electromagnetic force is the Maxwell tensor method, i.e., to first calculate the airgap flux density under one pole over one electrical period. Then, the radial electromagnetic force density is computed as:

$$F_r = \frac{B_r^2 - B_t^2}{2\mu_0} \approx \frac{B_r^2}{2\mu_0} \tag{1}$$

where μ_0 is the permeability of the air. B_r and B_t are radial and tangential flux densities in the airgap, respectively. Because the slot opening in the IPMSM [11] is small, the tangential component is neglected when calculating F_r in this paper.

According to the idea of CE-FEA [24], the flux density in the stator over one electrical period can be reconstructed with the results obtained from 1/6 electrical period by fully exploiting the symmetries of electric and magnetic circuits, which is obviously also applicable for the flux density in the airgap layer near the stator. Here, another method for achieving the CE-FEA is introduced based on the *dq* transformation. For clearly illustrating this method, the airgap flux density under one pole over one electrical period is first analyzed. As shown in Fig. 2, it is assumed that there are N points under one pole for sampling the flux density, where N is the integer multiple of 3. Then, the points from 1 to $N/3$ belongs to the $+A$ phase belt, points from $N/3+1$ to $2N/3$ belongs to the $-C$ phase belt, and points from $2N/3+1$ to N belongs to the $+B$ phase belt, where ABC is used to denote the three-phase system. In this case, point i ($1 \leqslant i \leqslant N/3$), point $i+N/3$, and point $i+2N/3$ form a three-phase system.

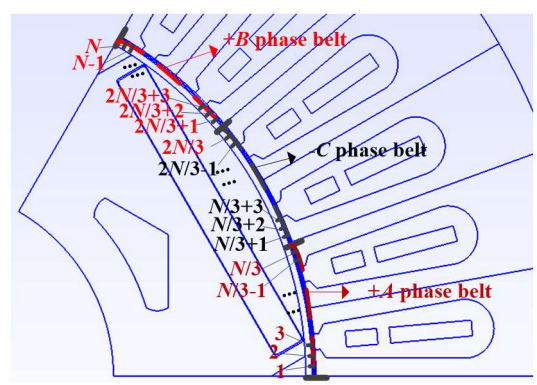

Fig. 2. N uniformly distributed points for calculating flux density.

For example, Fig. 3 shows the radial flux density B_r^1 at point 1, $B_r^{2N/3+1}$ at point $2N/3+1$, and the opposite of the flux density $B_r^{N/3+1}$ at point $N/3+1$. They clearly form a three-phase system with a positive sequence. Hence, the *dq* transformation can be applied to obtain the flux density in the rotor reference frame as:

$$\begin{bmatrix} f_d \\ f_q \\ f_0 \end{bmatrix} = \frac{2}{3}\begin{bmatrix} \cos\theta_e & \cos(\theta_e - 2\pi/3) & \cos(\theta_e + 2\pi/3) \\ -\sin\theta_e & -\sin(\theta_e - 2\pi/3) & -\sin(\theta_e + 2\pi/3) \\ 1/\sqrt{2} & 1/\sqrt{2} & 1/\sqrt{2} \end{bmatrix}\begin{bmatrix} f_A \\ f_B \\ f_C \end{bmatrix} \tag{2}$$

$$\theta_e = \theta_{er} + \theta_i = p\theta_m + \theta_i \tag{3}$$

where θ_m is the rotor mechanical angle, p is the number of pole pairs, θ_{er} is the rotor electrical angle. θ_e is the electrical angle of the d-axis ahead of the A-axis and θ_e is equal to θ_i when θ_m is 0, as shown in Fig. 4. f_A, f_B, and f_C are three-phase quantities in the stator reference frame, while f_d, f_q, and f_0 are corresponding quantities in the dq reference frame.

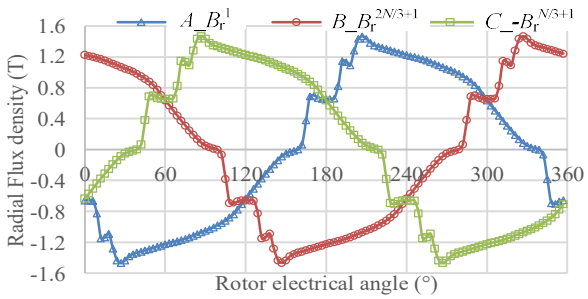

Fig. 3. Flux density waveforms at three points forming a three-phase system.

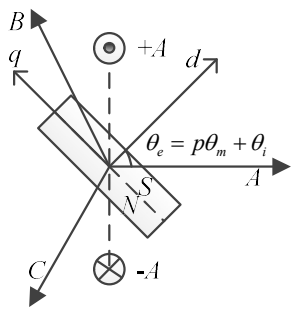

Fig. 4. Diagram of dq transformation.

Fig. 5 shows the calculated flux density waveforms in the dq reference frame when submitting the three-phase flux densities in Fig. 3 into

(2). θ_i is 165° for the IPMSM in this paper. It can be clearly seen that:

$$B_d(\theta_{er} + l\cdot 60^o) = B_d(\theta_{er}), \quad l = 1,2,3,4,5, \quad 0 \le \theta_{er} < 60^o \tag{4}$$

$$B_q(\theta_{er} + l\cdot 60^o) = B_q(\theta_{er}), \quad l = 1,2,3,4,5, \quad 0 \le \theta_{er} < 60^o \tag{5}$$

$$B_0(\theta_{er} + l\cdot 60^o) = \begin{cases} -B_0(\theta_{er}), & l = 1,3,5, \quad 0 \le \theta_{er} < 60^o \\ B_0(\theta_{er}), & l = 2,4 \quad 0 \le \theta_{er} < 60^o \end{cases} \tag{6}$$

where B_d, B_q, and B_0 are flux densities at d-, q-, and 0-axis respectively. Hence, the flux density waveforms in the dq reference frame over one electrical period can be directly obtained by repeating the waveforms obtained in the first 60°.

After obtaining the flux densities in the dq reference frame over one electrical period, the flux densities in the stator reference frame can be calculated by applying the inverse dq transformation as:

$$\begin{bmatrix} f_A \\ f_B \\ f_C \end{bmatrix} = \begin{bmatrix} \cos\theta_e & -\sin\theta_e & 1/\sqrt{2} \\ \cos(\theta_e - 2\pi/3) & -\sin(\theta_e - 2\pi/3) & 1/\sqrt{2} \\ \cos(\theta_e + 2\pi/3) & -\sin(\theta_e + 2\pi/3) & 1/\sqrt{2} \end{bmatrix}\begin{bmatrix} f_d \\ f_q \\ f_0 \end{bmatrix} \tag{7}$$

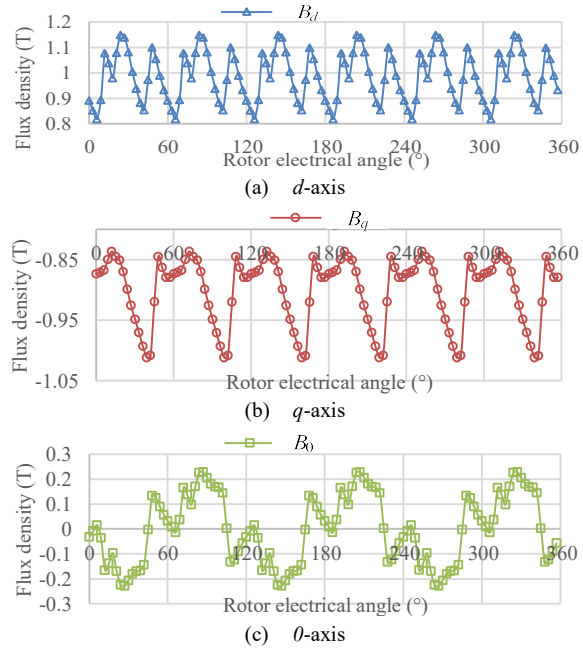

Fig. 5. Flux density waveforms in the dq reference frame.

The above procedure can be repeated when i increases from 1 to N/3, so that the flux densities at N points under one pole over one electrical period can be calculated with those obtained in 1/6 electrical period. For the prototype machine, N is chosen as 144. Fig. 6 compares the flux densities at three arbitrarily chosen points calculated with common FEA over one electrical period and those reconstructed with the FEA results obtained in 60° based on the dq transformation. They agree with each other very well demonstrating the effectiveness of the proposed method.

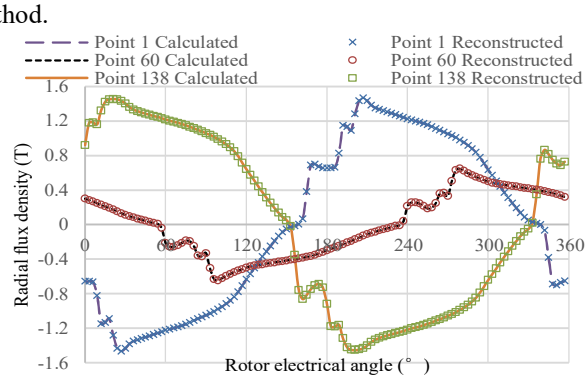

Fig. 6. Comparison of calculated and reconstructed flux densities at three arbitrarily chosen points.

B. *Fast Calculation of Airgap Flux Densities under Independent D- or Q-axis HFHV Excitation with THFEA*

PWM harmonic voltages can be viewed as the combination of a series of high-frequency components whose frequencies are usually near the integer multiples of the carrier frequency. With the FDRTM, the IPMSM model can be linearized and THFEA can be utilized to investigate the relationships between HFHVs and high-frequency flux densities in PMs and SSTs [21]-[23]. It is a natural idea that this method can also be applied to investigate the high-frequency flux densities in the airgap. According to [21]-[23], the PWM-induced losses in PMs and SSTs can be fast calculated with the THFEA results under

independent d- and q-axis HFHV excitations. Hence, in this Sub-section, the same THFEA results are utilized to investigate the relationships between HFHVs and airgap flux density variations without repeating more THFEA. The relationship between the injected three-phase HFHVs for the THFEA and the d- and q-axis HFHVs at different rotor positions can be expressed as [21]:

$$\begin{bmatrix} \boldsymbol{v}_{Ah} \\ \boldsymbol{v}_{Bh} \\ \boldsymbol{v}_{Ch} \end{bmatrix} = \begin{bmatrix} \cos(\theta_e) & -\sin(\theta_e) \\ \cos(\theta_e - 2\pi/3) & -\sin(\theta_e - 2\pi/3) \\ \cos(\theta_e + 2\pi/3) & -\sin(\theta_e + 2\pi/3) \end{bmatrix} \begin{bmatrix} \boldsymbol{v}_{dh} \\ \boldsymbol{v}_{qh} \end{bmatrix} \tag{8}$$

where $\boldsymbol{v}_{dh}$ and $\boldsymbol{v}_{qh}$ are d- and q-axis HFHVs, respectively. Note that the frequency of $\boldsymbol{v}_{dh}$ and $\boldsymbol{v}_{qh}$ is the same as that of $\boldsymbol{v}_{Ah}$, $\boldsymbol{v}_{Bh}$, and $\boldsymbol{v}_{Ch}$ because the rotor is assumed to be stationary in the THFEA. This transformation is named as the stationary dq transformation because the rotor speed is assumed as 0, although the d- and q-axes rotate with the rotor. The 0 sequence HFHVs are neglected because the three-phase windings are connected in the Y style.

The airgap flux densities under one pole when $\boldsymbol{v}_{dh}$ or $\boldsymbol{v}_{qh}$ is applied independently are first calculated at different rotor positions with the small-signal THFEA. In the calculation, they are all assumed as $40e^{j0}$V and their frequencies are set as 4200 Hz, which is equal to f_c+4f_o. To obtain the high-frequency flux densities over one fundamental electrical period, the reconstruction method based on the dq transformation presented in Section II-A is also applied so that only the flux densities while the rotor rotates over 1/6 electrical period needs to be calculated. Taking point 1 in Fig. 2 as an example, Fig. 7(a) and (b) compare real and imaginary parts of the flux densities at this point calculated over one electrical period and those reconstructed with the THFEA results over 1/6 electrical period under $\boldsymbol{v}_{dh}$ or $\boldsymbol{v}_{qh}$ independent excitation, respectively. $B_{sd0}^{C_r}$ and $B_{sd0}^{R_r}$ are the calculated and reconstructed real parts of the airgap flux densities under $\boldsymbol{v}_{dh}$ excitation, respectively, while $B_{sq0}^{C_r}$ and $B_{sq0}^{R_r}$ are those obtained under $\boldsymbol{v}_{qh}$ excitation. Meanwhile, $B_{sd0}^{C_i}$ and $B_{sd0}^{R_i}$ represent the calculated and reconstructed imaginary parts under $\boldsymbol{v}_{dh}$ excitation, respectively, while $B_{sq0}^{C_i}$ and $B_{sq0}^{R_i}$ are those obtained under $\boldsymbol{v}_{qh}$ excitation. Obviously, the calculated and reconstructed flux densities agree with each other very well, hence the reconstruction method shown in section II-A can also be applied for the complex flux densities. The same conclusion can be obtained at the other N-1 points in the airgap, which is no longer repeated here. The airgap flux densities obtained under independent $\boldsymbol{v}_{dh}$ and $\boldsymbol{v}_{qh}$ excitations form the foundation for fast calculating the flux densities generated by arbitrary HFHVs.

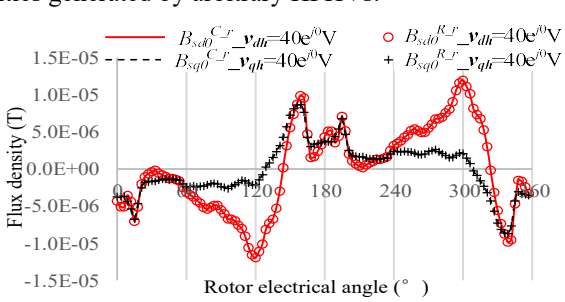

(a) Real part

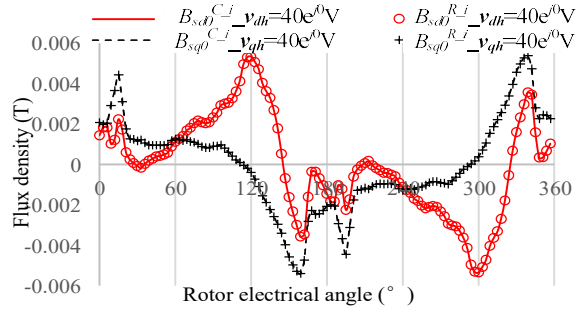

(b) Imaginary part

Fig. 7. Comparison of calculated and reconstructed complex flux densities under $\boldsymbol{v}_{dh}$ or $\boldsymbol{v}_{qh}$ independent excitation at point 1 when the frequency is 4200Hz

C. Calculation of High-Frequency Densities Caused by One Rotational HFHV

Before introducing the method for computing flux densities causing by all HFHVs in the PWM voltage spectra, the airgap flux densities caused by one rotational HFHV is first calculated based on the results obtained in section II-B and compared with those calculated using the traditional TSFEA method. It is assumed that a rotational HFHV with a positive sequence is injected into the machine together with the fundamental currents. However, it is impossible to use the three-phase current source and three-phase voltage source at the same time for conducting the TSFEA. Hence, the sum of the fundamental voltage and the HFHV is used as the input to conduct the TSFEA, which is expressed as:

$$\begin{aligned} v_A(t) &= V_1\cos(2\pi f_o t + \varphi_1) + V_h\cos(2\pi f_h t + \varphi_h) \\ v_B(t) &= V_1\cos(2\pi f_o t + \varphi_1 - 2\pi/3) + V_h\cos(2\pi f_h t + \varphi_h - 2\pi/3) \\ v_c(t) &= V_1\cos(2\pi f_o t + \varphi_1 + 2\pi/3) + V_h\cos(2\pi f_h t + \varphi_h + 2\pi/3) \end{aligned} \tag{9}$$

where V_1 and φ_1 are amplitude and initial phase angle of the applied fundamental voltage in phase A, respectively, which are determined from the TSFEA results under SCS supply [25]. V_h, f_h, and φ_h are amplitude, frequency, and phase angle of the injected HFHV, respectively. In this subsection, f_h is also assumed as f_c+4f_o, V_h is 40V, and φ_h is 0.

When conducting the TSFEA under voltage source supplies, the first step TSFEA still needs be conducted under SCS supply using the initial three-phase currents as input to minimize the transition process, so that one electrical period calculation is enough to analyze the steady-state characteristics [11]. From the second step on, voltage sources are used as the input for the calculation. When the backward Euler method is used to approximate the differential operation and the voltage drop in the resistance is neglected, the numerical voltage applied at θ_e is expressed as:

$$v^n(\theta_e) = \frac{\Psi(\theta_e) - \Psi(\theta_e - \Delta\theta_e)}{\Delta t} \approx v^a(\theta_e - \Delta\theta_e/2) \tag{10}$$

where Ψ represents the flux linkage which varies with θ_e, Δt is the time step of the TSFEA, $\Delta\theta_e$ is the variation of rotor electrical angle during Δt. v^a represents the analytical voltage shown in (9). It can be seen from (10) that there exists a phase difference of $\Delta\theta_e/2$ between the numerical voltage and the analytical one. For example, the numerical voltage applied at the second step TSFEA when rotor is located at $\Delta\theta_e$ should be

the analytical voltage at $\Delta\theta_e/2$. Hence, the numerical three-phase voltages applied for conducting the TSFEA are:

$$\begin{aligned} v_A^n(t) &= V_1\cos\left(2\pi f_o t+\varphi_1-\Delta\theta_e/2\right) \\ &+V_h\cos\left(2\pi f_h t+\varphi_h-\Delta\theta_e f_h/\left(2f_0\right)\right) \\ v_B^n(t) &= V_1\cos\left(2\pi f_o t+\varphi_1-2\pi/3-\Delta\theta_e/2\right) \\ &+V_h\cos\left(2\pi f_h t+\varphi_h-2\pi/3-\Delta\theta_e f_h/\left(2f_0\right)\right) \\ v_C^n(t) &= V_1\cos\left(2\pi f_o t+\varphi_1+2\pi/3-\Delta\theta_e/2\right) \\ &+V_h\cos\left(2\pi f_h t+\varphi_h+2\pi/3-\Delta\theta_e f_h/\left(2f_0\right)\right) \end{aligned} \tag{11}$$

It can be seen form (11) that the phase difference for the HFHV whose frequency is f_h becomes $\Delta\theta_e f_h/2/f_o$, which will increase with f_h when $\Delta\theta_e$ is fixed.

For the THFEA analysis, the positive sequence HFHV in (9) can be transferred to the *dq* reference frame using the static *dq* transformation by substituting it into

(2), which is shown as:

$$\begin{bmatrix} v_{dh}(t) \\ v_{qh}(t) \end{bmatrix} = \begin{bmatrix} V_h\cos\left(2\pi f_h t+\varphi_h-\theta_e\right) \\ V_h\cos\left(2\pi f_h t+\varphi_h-\theta_e-\pi/2\right) \end{bmatrix} \tag{12}$$

where v_{dh}(t) and v_{qh}(t) are transient harmonic voltages at *d*- and *q*-axes, respectively. In (12), θ_e varies with the rotor position but is not considered as a function of *t*, hence the frequency of $v_{dh}(t)$ and $v_{qh}(t)$ is still f_h. For conducting the THFEA, $v_{dh}(t)$ and $v_{qh}(t)$ can be written in complex phasors, which are shown as:

$$\boldsymbol{v_{dh}} = V_h e^{j(2\pi f_h t+\varphi_h-\theta_e)}, \quad \boldsymbol{v_{qh}} = V_h e^{j(2\pi f_h t+\varphi_h-\theta_e-\pi/2)} \tag{13}$$

Assuming that in one electrical period, there are N_s sample points, which means there are N_s steps TSFEA under SCS supply and N_s steps corresponding small-signal THFEA. Hence, the *d*- and *q*-axis HFHVs applied for the THFEA at step *k* ($1\le k\le N_s$) can be expressed as:

$$\boldsymbol{v_{dh}} = V_h e^{j\left(\frac{2\pi(k-1)f_h}{f_o N_s}+\varphi_h-\theta_e\right)}, \quad \boldsymbol{v_{qh}} = V_h e^{j\left(\frac{2\pi(k-1)f_h}{f_o N_s}+\varphi_h-\theta_e-\pi/2\right)} \tag{14}$$

where *k* is an integer. It can be seen from (14) that the phase angle of $\boldsymbol{v_{dh}}$ and $\boldsymbol{v_{qh}}$ vary as the rotor rotates. Rather than conducting the THFEA to calculate the flux densities caused by the combination of $\boldsymbol{v_{dh}}$ and $\boldsymbol{v_{qh}}$, they can be directly calculated with the results obtained in Section II-*B*, which is shown as:

$$\boldsymbol{B_h} = \frac{V_h \boldsymbol{\chi_{sd0}}}{f_h} e^{j\left(\frac{2\pi(k-1)f_h}{f_o N_s}+\varphi_h-\theta_e\right)} + \frac{V_h \boldsymbol{\chi_{sq0}}}{f_h} e^{j\left(\frac{2\pi(k-1)f_h}{f_o N_s}+\varphi_h-\theta_e-\pi/2\right)} \tag{15}$$

$$\boldsymbol{\chi_{sd0}} = \frac{\boldsymbol{B_{sd0}}\left(\alpha,\theta_{er}\right)\cdot f_s}{V_s}, \quad \boldsymbol{\chi_{sq0}} = \frac{\boldsymbol{B_{sq0}}\left(\alpha,\theta_{er}\right)\cdot f_s}{V_s} \tag{16}$$

where α is the distribution angle along the inner surface of the stator. $\boldsymbol{B_{sd0}}(\alpha, \theta_{er})$ are flux densities obtained from the small-signal THFEA using the *d*-axis HFHV $V_s e^{j0}$ as input, whose frequency is f_s. Similarly, $\boldsymbol{B_{sq0}}(\alpha, \theta_{er})$ are those obtained from the THFEA using the *q*-axis HFHV $V_s e^{j0}$ as input, whose frequency is also f_s. The real and imaginary parts of $\boldsymbol{B_{sd0}}$ and $\boldsymbol{B_{sq0}}$ has been calculated in Section II-*B* when V_s is 40V and f_s is f_c+4f_o. $\boldsymbol{\chi_{sd0}}$ and $\boldsymbol{\chi_{sq0}}$ are two constant matrices when neglecting eddy current reaction effects at one fixed working condition, because the flux density is proportional to the voltage amplitude and inversely proportional to the frequency [21]-[23]. Besides, the simple superposition principle can be applied because the model has been linearized with the FDRTM. When considering more working conditions and the eddy current reaction effects, $\boldsymbol{\chi_{sd0}}$ and $\boldsymbol{\chi_{sq0}}$ will be functions of i_d, i_q, and frequency, which can be modeled with interpolation methods and more THFEA considering the eddy current reaction effect [21]-[23].

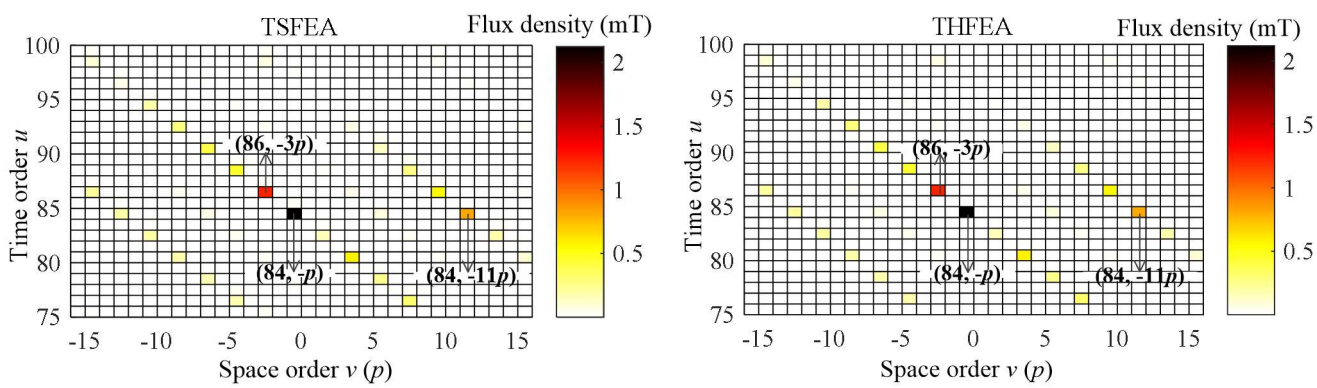

(a) TSFEA (b) Small-signal THFEA

Fig. 8. Comparison of the flux density spectra caused by one rotational HFHV calculated with different methods.

After obtaining the flux densities under one pole, they can be simply extended to calculate those under one pole pairs by exploiting the symmetry characteristics of the flux density. Then, 2D FFT can be applied to calculate the spectra of the flux density caused by the combination of $\boldsymbol{v_{dh}}$ and $\boldsymbol{v_{qh}}$. On the other hand, 2D FFT can also be applied to obtain the spectra of the flux densities calculated with the traditional TSFEA using (11) as input. When conducting the TSFEA, there are 2000 steps in one fundamental period and there are about 28.3 sample points in one high-frequency period. Fig. 8 compares the spectra of the flux densities calculated with different methods, which are caused by the positive rotational HFHV shown in (9). Clearly, a series of flux density harmonic components are generated and they agree with each other very well. The preponderant components are (u=84, v=-p) and (u=86, v=-3p), because f_h is 84 times of f_o. The other components attenuate as they become further away from the preponderant components. Table I further compares several preponderant components in Fig. 8 quantitatively, which demonstrates that (15)-(16) can be effectively applied for calculating the high-frequency airgap flux density.

TABLE I
COMPARISON OF PREPONDERANT COMPONENTS IN FLUX DENSITY SPECTRA OBTAINED WITH DIFFERENT METHODS CAUSED BY ONE HFHV

Time order	Space order	Amplitude (mT)		Phase angle (°)	
u	v (p)	TSFEA	THFEA	TSFEA	THFEA
84	-1	2.124	2.119	-165.0	-165.2
86	-3	1.225	1.221	-68.4	-68.5
84	11	0.804	0.802	-163.1	-163.2
82	1	0.146	0.142	-144.4	-145.8
80	3	0.572	0.569	-141.1	-140.6
86	9	0.547	0.546	-76.7	-76.6

D. *Fast Calculation of High-Frequency Flux density Spectra Caused by All PWM-Induced HFHVs*

The method shown in Section II-*C* can be further extended to calculate the high-frequency flux density spectra caused by all the PWM-induced HFHVs based on the superposition principle. The PWM voltage spectra can be generated analytically or numerically [21], [25]. In this paper, the PWM voltages are generated with the numerical method shown in [25]. The space vector pulse width modulation (SVPWM) method is used, and there are 4000 steps in one fundamental period and hence 50 steps in one carrier period to distinguish the HFHVs in the PWM voltages. Then, the three-phase PWM voltages are first analyzed with the FFT to calculate the spectra of each phase, which are then substituted into

(2) to conduct the static dq transformation, with which θ_e is considered as independent of t. Unlike the rotational dq transformation in the rotor reference frame or the static $\alpha\beta$ transformation in the stator reference frame [22], the spectra of the PWM voltages vary with the rotor position. For example, according to (12), the phase angle of a rotational HFHV with the positive sequence at the static dq reference frame decreases with the increase of θ_e, although the amplitudes of $v_{dh}(t)$ and $v_{qh}(t)$ keep unchanged.

Assuming that the PWM-induced HFHVs in the static d- and q- axes are denoted as $V_{dh}e^{j\varphi_{dh}}$ and $V_{qh}e^{j\varphi_{qh}}$, respectively, where V_{dh} and V_{qh} are amplitudes and φ_{dh} and φ_{qh} are phase angles at different θ_e. Fig. 9 shows V_{dh} and V_{qh} when θ_m is 0, which is similar to the PWM voltage spectra obtained from the static $\alpha\beta$ transformation [22]. Components with the frequencies of f_c-$2f_o$, f_c+$4f_o$, $2f_c$+f_o, and $3f_c$-$2f_o$ have the positive sequence, while those with the frequencies of f_c-$4f_o$, f_c+$2f_o$, $2f_c$-f_o and $3f_c$+$2f_o$ have the negative sequence [8]. Fig. 10 shows the variations of φ_{dh} and φ_{qh} with θ_{er} for two positive and negative components. For the component with a positive sequence, φ_{qh} always lags φ_{dh} by 90°, and they both decrease as θ_{er} increases. For the negative component, φ_{qh} is always 90° leading φ_{dh}, and they both increase with θ_{er}.

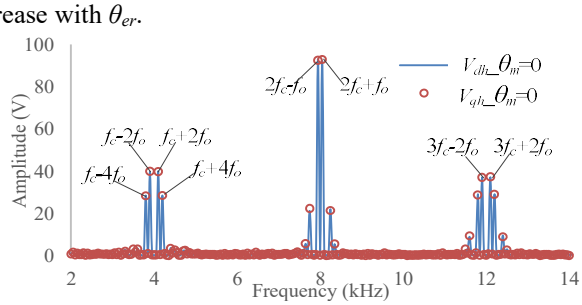

Fig. 9. Amplitudes of each HFHV in the static dq coordinate when θ_m is 0.

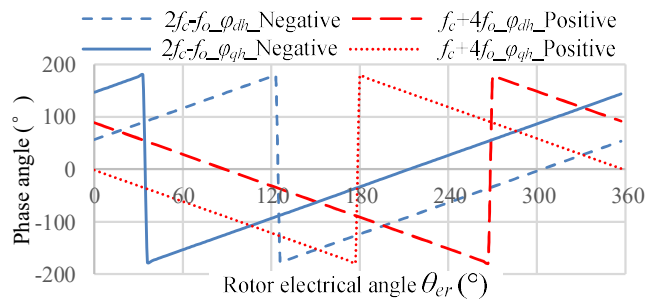

Fig. 10. Variations of φ_{dh} and φ_{qh} with θ_{er} for different components.

Similar to (15), the flux density generated by each HFHV can be calculated as:

$$\boldsymbol{B_h} = \frac{V_{dh}\boldsymbol{\chi_{sd0}}}{f_h} e^{j\left(\frac{2\pi(k-1)f_h}{f_o N_s}+\varphi_{dh}\right)} + \frac{V_{qh}\boldsymbol{\chi_{sq0}}}{f_h} e^{j\left(\frac{2\pi(k-1)f_h}{f_o N_s}+\varphi_{qh}\right)} \tag{17}$$

where f_h is the frequency of the HFHV. 2D FFT is then applied for calculating the spectral of the flux density caused by this HFHV. After that, the flux density spectra caused by each HFHV is superimposed in the frequency domain to obtain the flux density spectra caused by all the HFHVs.

To correctly superimpose the flux density spectra caused by each HFHV, several important points to be addressed are listed as follows. First, the time order of the flux density component, no matter how high its frequency is, obtained from the 2D FFT of the complex flux densities in (17) will always fall in the range between 0 and N_s-1 because there are N_s sample points in one fundamental electrical period. Hence, the flux density spectra directly obtained from the 2D FFT need to be modified for conducting the superposition. To clearly demonstrate the modified method, the flux density spectra caused by the HFHV component whose frequency is $3f_c$-$2f_o$ is taken as an example for the illustration. Because $3f_c$-$2f_o$ is 238 times of f_o, the time order of the maximum flux density component should be also 238 according to Fig. 8. However, the time order of this component becomes 118 in the directly obtained spectra, as shown in Fig. 11(a). The other preponderant components must distribute around this component, which is similar to Fig. 8. However, the component whose time order should be 240 becomes the 0 in Fig. 11(a). Hence, the modification process for the flux density spectra caused by the voltage component whose frequency is f_h can be expressed as:

$$\boldsymbol{B}_{\mathbf{mod}}(i_T) = \boldsymbol{B}_{\boldsymbol{ini}}\left(\mathrm{mod}(i_T, N_s)\right), \quad \frac{f_h}{f_o} - \frac{N_s}{2} \le i_T \le \frac{f_h}{f_o} + \frac{N_s}{2} - 1 \tag{18}$$

where i_T denotes the time orders of the flux density components caused by the f_h harmonic voltage, which are assumed to be within f_h/f_o-$N_s/2$ and f_h/f_o+$N_s/2$-1. The function mod(i_T, N_s) means the remainder after division of i_T by N_s. $\boldsymbol{B_{ini}}$ represents the initial spectra directly obtained from the 2D FFT, as shown in Fig. 11(a). $\boldsymbol{B_{mod}}$ represents the right flux density spectra, as shown in Fig. 11(b), which can be calculated with the modification method shown in (18).

The flux density spectra caused by each component in the PWM-induced HFHVs can be obtained from the above procedure. Then, the superposition method can be applied for

calculating the total spectra caused by all the HFHVs. In this case, the harmonic voltage components ranging from 2.5kHz to 25kHz are submitted into (17) to calculate the flux density spectra. Fig. 12 and Fig. 13 compare the flux density spectra calculated with the traditional TSFEA method and the proposed method. When conducting the TSFEA, SVPWM voltages are used as the input to conduct 4000-step transient calculations in one electrical period to compute the flux density waveforms [21]-[23], [25]. Then, 2D FFT is applied to obtain their spectra. Obviously, the spectra obtained from the two methods agree with each other very well.

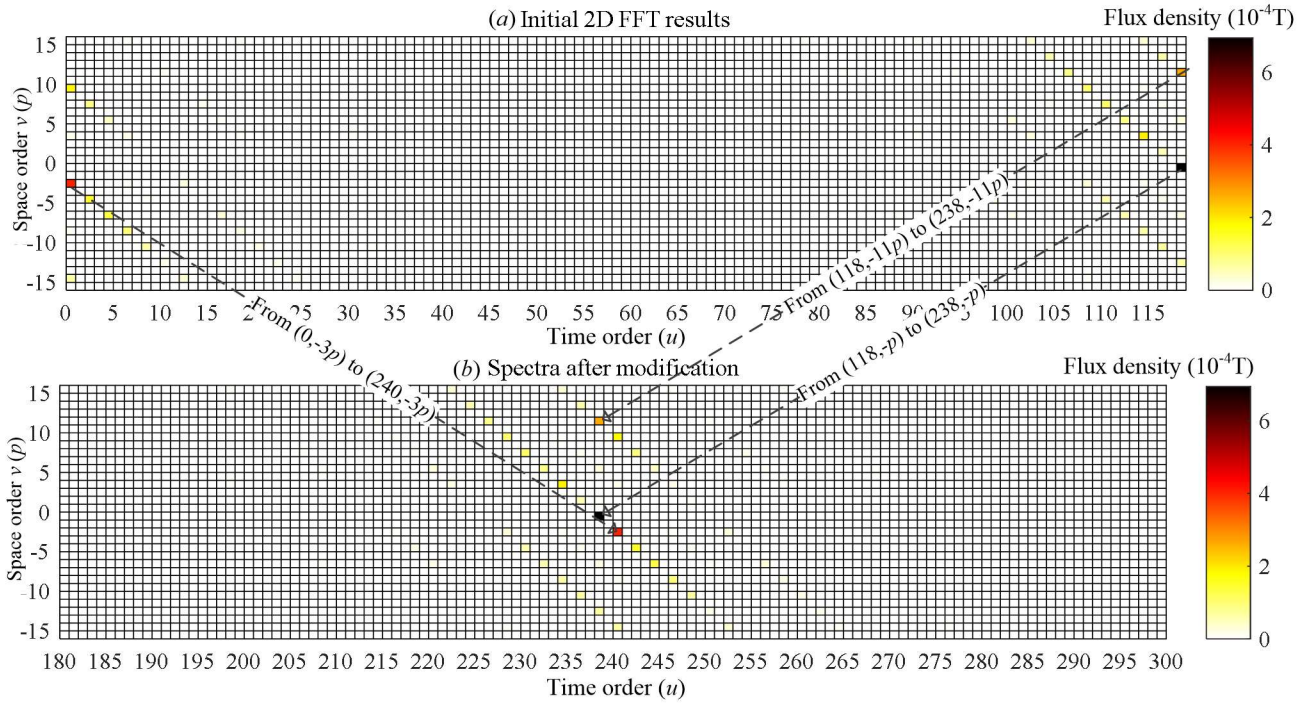

Fig. 11. Illustration of the flux density spectra modification procedure for those caused by the $3f_c$-$2f_o$ HFHV

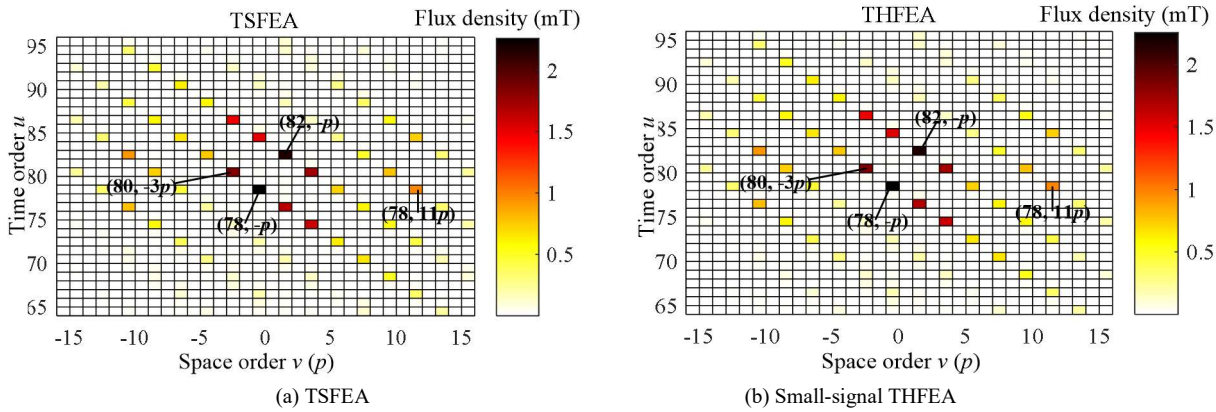

Fig. 12. Flux density spectra around f_c.

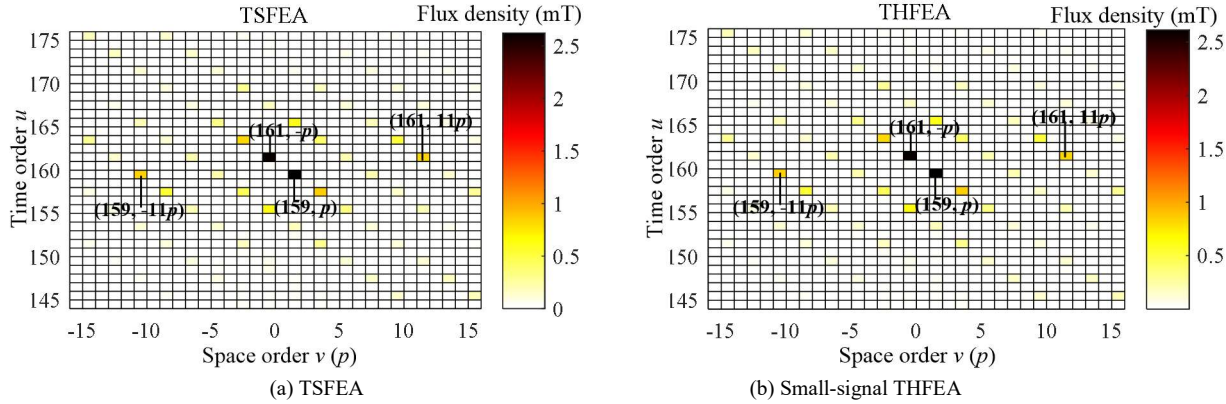

Fig. 13. Flux density spectra around $2f_c$.

TABLE II
COMPARISON OF PREPONDERANT COMPONENTS IN THE FLUX DENSITY SPECTRA OBTAINED WITH DIFFERENT METHODS UNDER PWM VSI SUPPLY

Time order u	Space order v (p)	Amplitude (mT) TSFEA	THFEA	Phase angle (°) TSFEA	THFEA	Difference
78	-1	2.258	2.256	-16.2	-19.5	-3.3
78	11	0.970	0.969	-22.0	-25.3	-3.3
80	-3	1.824	1.820	75.5	71.9	-3.6
82	1	2.149	2.147	-157.0	-160.9	-3.9
159	-11	0.827	0.825	-127.8	-134.9	-7.1
159	1	2.624	2.613	-112.3	-119.5	-7.2
161	-1	2.588	2.577	-53.4	-60.6	-7.1
242	1	0.681	0.678	30.0	19.4	-10.6
321	-1	0.609	0.600	-46.2	-60.4	-14.2

For a quantitative comparison, both amplitudes and phase angles of several preponderant components are shown in Table II. It can be seen that the amplitudes agree with each other very well. However, there exist errors in the phase angles, which increase with the increase of the time order. This is because the PWM voltages are generated numerically and submitted for conducting the TSFEA without modifying the phase angle of each component using (11). Numerical errors generated because of the backward Euler method used to approximate the differential operation, which has been explained in Section II-*C*. It will be shown in the next subsection that the phase angle errors will not result in significant errors in the magnetic forces, which are the sources of vibrations and noises.

III. CALCULATION OF ELECTROMAGNETIC FORCE SPECTRA WITH FLUX DENSITY SPECTRA

The total flux density spectra under PWM VSI supply can be obtained with the sum of those calculated under SCS supply in Section II-*A* and those caused by HFHVs in Section II-*D*, which is expressed in the frequency domain as:

$$B_r = \sum_{u=0}^{N_u} \sum_{v=-N_v/2}^{N_v/2} B_{uv} \cos\left(u\omega_o t + vp\theta_m + \varphi\right) \tag{19}$$

$$\omega_o = 2\pi f_o \tag{20}$$

where N_u is the maximum time order and $pN_v/2$ is the maximum space order. B_{uv} and φ are the amplitude and phase angle of the component (u, vp). ω_o is the fundamental angular frequency. By submitting (19) into (1), the PWM-induced electromagnetic force spectra can be calculated analytically as:

$$\begin{aligned} F_r &= \sum_{k=0}^{N_k} \sum_{l=-N_l/2}^{N_l/2} F_{kl} \cos\left(k\omega_o t + lp\theta_m + \varphi_{kl}\right) = \frac{1}{2\mu_0} \sum_{u_1=0}^{N_u} \sum_{v_1=-N_v/2}^{N_v/2} \sum_{u_2=0}^{N_u} \sum_{v_2=-N_v/2}^{N_v/2} B_{u1v1} B_{u2v2} \cos\left(u_1\omega_o t + v_1 p\theta_m + \varphi_1\right) \\ &\quad \cdot \cos\left(u_2\omega_o t + v_2 p\theta_m + \varphi_2\right) \\ &= \frac{1}{2\mu_0} \sum_{u_1=0}^{N_u} \sum_{v_1=-N_v/2}^{N_v/2} \sum_{u_2=0}^{N_u} \sum_{v_2=-N_v/2}^{N_v/2} B_{u1v1} B_{u2v2} \cos\left((u_1+u_2)\omega_o t + (v_1+v_2)p\theta_m + \varphi_1 + \varphi_2\right) \\ &\quad + B_{u1v1} B_{u2v2} \cos\left((u_1-u_2)\omega_o t + (v_1-v_2)p\theta_m + \varphi_1 - \varphi_2\right) \end{aligned} \tag{21}$$

where k and l are integers, which denote the time and space order of the electromagnetic forces, respectively. F_{rl} and φ_{kl} are amplitudes and phase angles of the component (k, lp), respectively. N_k and $pN_l/2$ are the maximum time and space orders of the electromagnetic force spectra, respectively. The subscripts $_1$ and $_2$ are used to distinguish the two multiplied components.

Theoretically, it is straightforward to compute F_{kl} of each component according to (21). However, a quadruple cycle is needed in the program, which makes it very time-consuming for computing the electromagnetic forces generated by all the flux density components. Fortunately, for the PWM-induced high-frequency force components, only those with low space orders are important for the vibration and noise calculation [8]. In this case, N_k is set as 400, which is corresponding to the highest audible frequency. N_l is set as 36 so that the maximum space order of the force is 54 (18p). N_u is set as 560 and N_v is 72, which are larger than N_k and N_l because some high-order flux density components may also contribute to low-order force components [20]. The high-frequency force density spectra calculated with different methods are compared in Fig. 14 and Fig. 15. Obviously, they agree with each other very well. For a quantitative comparison, the amplitudes of several components are shown in Table III. The relative errors between the traditional TSFEA and the proposed method are with 3.1% at 11 preponderant components, which shows that the proposed method has rather good accuracy for engineering applications. The possible reasons for the errors are summarized as follows. (1) The phase resistance makes the assumption that the voltage is proportional to the flux density no longer true when the frequency is low. (2) The PWM flux density harmonics may also contribute to the saturation in the SSTs, which is assumed to be only determined by the fundamental current with the FDRTM. (3) The Phase angle difference between the high-frequency flux densities calculated with the proposed method and the traditional TSFEA shown in Table II may also cause the error in the calculated electromagnetic force. Besides, the used traditional TSFEA may also has errors when compared with the experiment results [11]. More researches in the future are still needed to conduct the experimental verification. By the way, it is suggested to use the transient flux density waveforms obtained under SCS supply for computing the force density spectra caused by fundamental currents and the PM, rather than using (21), because the investigated maximum space order of the low-frequency force components is usually high. In this case, using (21) will be time-consuming.

Table IV compares the calculation time of the traditional TSFEA and the proposed method. The FEA model in this paper has 12864 nodes and 24606 first order triangular elements and the calculation is conducted in a personal computer with an Intel Core i7-9750H CPU @ 2.60GHz. With the traditional method, 4000 steps nonlinear TSFEA are needed, which takes 46min. Additional 46s is needed for 2D FFT to calculate the force

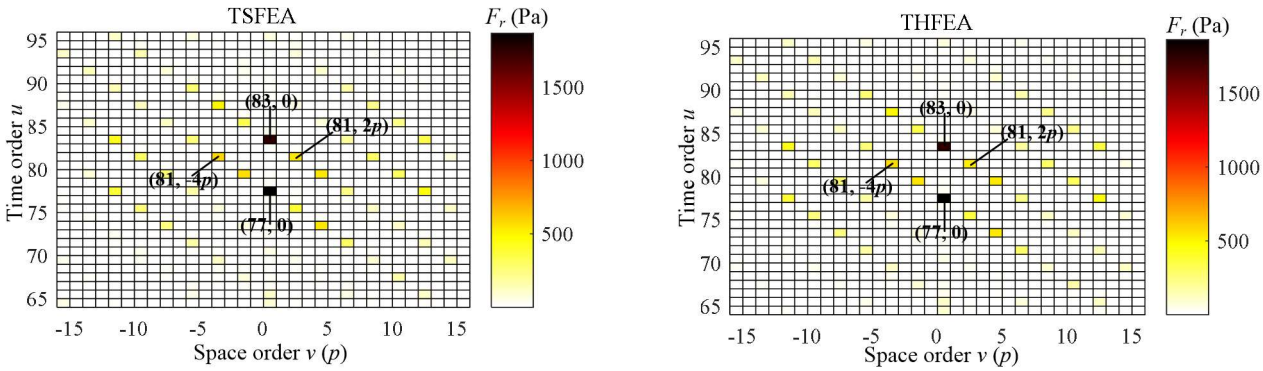

(a) TSFEA (b)Small-signal THFEA

Fig. 14. Force density spectra around f_c.

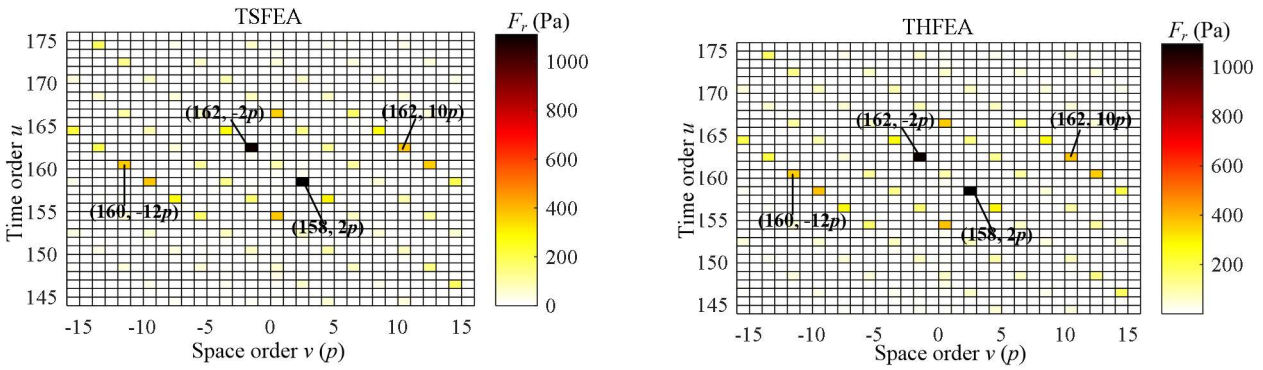

(a) TSFEA (b) Small-signal THFEA

Fig. 15. Force density spectra around $2f_c$.

TABLE III
COMPARISON OF PREPONDERANT COMPONENTS IN FORCE DENSITY SPECTRA OBTAINED WITH DIFFERENT METHODS UNDER PWM VSI SUPPLY

Frequency	Time order u	Space order v (p)	Force density (Pa) TSFEA	Force density (Pa) THFEA	Relative Error
f_c-3f_o	77	0	1866.0	1860.8	-0.28%
f_c-f_o	79	-2	550.9	536.7	-2.57%
f_c+f_o	81	2	527.9	511.5	-3.10%
f_c+3f_o	83	0	1746.4	1742.3	-0.24%
2f_c-2f_o	158	2	1114.5	1095.3	-1.72%
2f_c	160	12	361.2	351.3	-2.75%
2f_c+2f_o	162	-2	1091.7	1081.2	-0.95%
3f_c-3f_o	237	0	589.7	582.6	-1.20%
3f_c-f_o	239	4	170.6	165.8	-2.82%
4f_c+2f_o	322	-2	266.8	261.0	-2.18%
4f_c+6f_o	326	0	251.7	246.1	-2.25%

density spectra. With the proposed method, only 42s is needed for the FEA. However, another 68s is still needed to use (21) for the force density spectra. By the way, when applying the proposed method for force density spectra calculations caused by other PWM voltages with different dc-bus voltages, carrier frequencies, or modulation strategies at the same working point, it is no longer to repeat 20 steps TSFEA and 40 steps THFEA, although additional time for the analytical force density spectra calculation is still needed.

TABLE IV
COMPARISON OF CALCULATION TIME WITH DIFFERENT METHODS

Methods	Traditional	Proposed
FEA calculation	4000 steps TSFEA	20 steps TSFEA+40 steps THFEA
FEA time	46 min	42 s
Additional Time	46 s	68 s

IV. CONCLUSION

This paper proposed a fast PWM-induced force density spectra calculation method for IPMSMs based on the small-signal THFEA. The detailed calculation procedure has been presented. The relative errors between the preponderant components with the proposed method and those obtained from the traditional TSFEA have been shown to be within 3.1%, while the proposed method improves the calculation speed for over 24 times at one working condition. Some conclusions can be drawn as follows.

(1) Based on the small-signal THFEA, the functional relationships between HFHVs and high-frequency flux densities in the airgap can be established with χ_{sd0} and χ_{sq0} without calculating HFHCs. Besides, χ_{sd0} and χ_{sq0} can be obtained together with z_{d1}, z_{d2}, z_{q1}, and z_{q2} in [21] as well as χ_{ds}, χ_{dr}, χ_{qs}, and χ_{qr} in [22] without additional THFEA.

(2) One HFHV component at f_h generates a series of high-frequency flux density components distributing around f_h. The time order modification using (18) on the initial spectra directly obtained from the 2D FFT is essential for obtaining the correct flux density spectra.

(3) The proposed method can be used for fast evaluating the influence of inverters' parameters on the high-frequency electromagnetic forces, as well as corresponding vibrations and noises, which will be investigated in the future.

REFERENCES

[1] Z. Yang, F. Shang, I.P. Brown, and M. Krishnamurthy, "Comparative study of interior permanent magnet, induction, and switched reluctance motor drives for EV and HEV applications," *IEEE Trans. Transp. Electrific.*, vol.

1, no. 3, pp. 245-254, Aug. 2015.

[2] H. Ge, B. Guo, X. Qiu, J. Yang, C. Feng, C. Bai, Z. Jin, and Y. Zhang, "Optimizing the flux barriers of interior permanent magnet machine for noise reduction under certain load conditions," *IET Electr. Power Appl.* vol. 15, no. 11, pp. 1512– 1528, 2021.

[3] M. Boesing, T. Schoenen, K. A. Kasper, and R. W. De Doncker, "Vibration synthesis for electrical machines based on force response superposition," *IEEE Trans. Magn.*, vol. 46, no. 8, pp. 2986–2989, Aug. 2010.

[4] Z. Wu, Y. Fan, H. Chen, X. Wang, and C. H. T. Lee, "Electromagnetic force and vibration study of dual-stator consequent-pole hybrid excitation motor for electric vehicles," *IEEE Trans. Veh. Technol.*, vol. 70, no. 5, pp. 4377–4388, May 2021.

[5] Y. Lu, J. Li, H. Xu, K. Yang, F. Xiong, R. Qu, and J. Sun, "Comparative study on vibration behaviors of permanent magnet assisted synchronous reluctance machines with different rotor topologies," *IEEE Trans. Ind. Appl.*, vol. 57, no. 2, pp. 1420–1428, Mar. 2021.

[6] H. Fang, D. Li, J. Guo, Y. Xu, and R. Qu, "Hybrid model for electromagnetic vibration synthesis of electrical machines considering tooth modulation and tangential effects", *IEEE Trans. Ind. Electron.*, vol. 68, no. 8, pp. 7284–7293, Aug. 2021.

[7] F. Lin, S. Zuo, W. Deng, and S. Wu, "Modeling and analysis of electromagnetic force, vibration, and noise in permanent-magnet synchronous motor considering current harmonics," *IEEE Trans. Ind. Electron.*, vol. 63, no. 12, pp. 7455–7466, Dec. 2016.

[8] T. Hara, T. Ajima, Y. Tanabe, M. Watanabe, K. Hoshino, and K. Oyama, "Analysis of vibration and noise in permanent magnet synchronous motors with distributed winding for the PWM method," *IEEE Trans. Ind. Appl.*, vol. 54, no. 6, pp. 6042–6049, Nov. 2018.

[9] S. Wu, W. Tong, W. Li, S. Yu, and R. Tang, "Electromagnetic vibration analysis of high-speed permanent magnet synchronous machines with amorphous metal stator cores considering current harmonics," *IEEE Trans. Ind. Electron.*, vol. 67, no. 12, pp. 10156–10167, Dec. 2020.

[10] I. Ibrahim, M. H. Mohammadi, V. Ghorbanian, and D. A. Lowther, "Effect of pulse-width modulation on electromagnetic noise of interior permanent magnet synchronous motor drives', *IEEE Trans. Magn.*, vol. 55, no. 10, pp. 1–5, Oct. 2019.

[11] S. Zhu, W. Hua, and B. Shi, "Comparison of methods using different sources for computing PWM effects on permanent magnet machines considering eddy current reaction," *IEEE Trans. Magn.*, vol. 57, no. 6, pp. 1-4, Jun. 2021.

[12] Z. Han and J. Liu, "Comparative analysis of vibration and noise in IPMSM considering the effect of MTPA control algorithms for electric vehicles," *IEEE Trans. Power Electron.*, vol. 36, no. 6, pp. 6850–6862, Jun. 2021.

[13] Y. Huang, Y. Xu, W. Zhang, and J. Zou, "Hybrid RPWM technique based on modified SVPWM to reduce the PWM acoustic noise," *IEEE Trans.* on *Power Electron.*, vol. 34, no. 6, pp. 5667–5674, Jun. 2019.

[14] X. Han, D. Jiang, T. Zou, R. Qu, and K. Yang, "Two-segment three-phase PMSM drive with carrier phase-shift PWM for torque ripple and vibration reduction," *IEEE Trans. Power Electron.*, vol. 34, no. 1, pp. 588–599, Jan. 2019.

[15] A. Andersson, D. Lennstrom, and A. Nykanen, "Influence of inverter modulation strategy on electric drive efficiency and perceived sound quality', *IEEE Trans. Transp. Electrific.*, vol. 2, no. 1, pp. 24–35, Mar. 2016.

[16] I. Tsoumas and H. Tischmacher, "Influence of the inverter's modulation technique on the audible noise of electric motors," *IEEE Trans. Ind. Appl.*, vol. 50, pp. 269–278, Jan. 2014.

[17] Y. Lv, S. Cheng, Z. Ji, D. Wang, and J. Chen, "Permeance distribution function: a powerful tool to analyze electromagnetic forces induced by PWM current harmonics in multiphase surface permanent-magnet motors," *IEEE Trans. Power Electron.*, vol. 35, no. 7, pp. 7379-7391, Jul. 2020.

[18] T. Liu, W. Zhao, J. Ji, S. Zhu, and D. Cao, "Effects of eccentric magnet on high-frequency vibroacoustic performance in integral-slot SPM machines," *IEEE Trans. Energy Convers.*, vol. 36, no. 3, pp. 2393-2403, Sep. 2021.

[19] W. Liang, P. C.-K. Luk, and W. Fei, "Analytical investigation of sideband electromagnetic vibration in integral-slot PMSM drive with SVPWM technique," *IEEE Trans. Power Electron.*, vol. 32, no. 6, pp. 4785-4795, Jun. 2017.

[20] J. Hong, S. Wang, Y. Sun, and H. Cao, "A high-precision analytical method for vibration calculation of slotted motor based on tooth modeling," *IEEE Trans. Ind. Appl.*, vol. 57, no. 4, pp. 3678-3686, 2021.

[21] S. Zhu, H. Wang, J. Zhang, Z. Lu, and M. Cheng, "Fast calculation of carrier harmonic loss in permanent magnet of IPMSM under PWM VSI supply over entire working range," *IEEE Trans. Energy Convers.*, vol. 34, no. 3, pp. 1581-1592, Sept. 2019.

[22] S. Zhu, J. Dong, Y. Li, and W. Hua, "Fast calculation of carrier harmonic iron losses caused by pulse width modulation in interior permanent magnet synchronous motors', *IET Electr. Power Appl.*, vol. 14, no. 7, Mar. 2020.

[23] S. Zhu and W. Hua, "Fast calculation of eddy current losses caused by pulse-width modulation in magnets of surface-mounted PM machines based on small-signal time-harmonic finite element analysis," *IET Electr. Power Appl.*, vol. 14, no. 11, pp. 2163–2170, Jul. 2020.

[24] G. Y. Sizov, D. M. Ionel, and N. A. O. Demerdash, 'Modeling and parametric design of permanent-magnet AC machines using computationally efficient finite-element analysis', *IEEE Trans. Ind. Electron.*, vol. 59, no. 6, pp. 2403–2413, Jun. 2012.

[25] K. Yamazaki and Y. Seto, "Iron loss analysis of interior permanent-magnet synchronous motors-variation of main loss factors due to driving condition," *IEEE Trans.* on *Ind. Appl.*, vol. 42, no. 4, pp. 1045-1052, Jul. 2006.

Sa Zhu (Member, IEEE) received the B.Sc. and Ph.D. degrees in electrical engineering from the School of Electrical Engineering, Southeast University, Nanjing, China, in 2011 and 2017, respectively.

From 2013 to 2014, he went to Politecnico di Torino for a one-year visiting study. Since 2017, he has been a Lecturer with Hohai University, Nanjing. His current research interests include permanent magnet machines, loss calculation, and multiphysics analysis.

Dr. Zhu holds the First Place in the 2011 IEEE Industry Applications Society Myron Zucker Undergraduate Student Design Contest.

Jianbo Lu received the B.E. degree in electrical engineering and automation from the School of Energy and Electrical Engineering, Hohai University, Nanjing, China, in 2021. He is currently working toward the M.E. degree in electrical engineering with the College of Energy and Electrical Engineering, Hohai University.

His current research interests include permanent magnet machines and finite element analysis.

Feng Zeng received the B.E. degree in electrical engineering and automation from the School of Energy and Electrical Engineering, Hohai University, Nanjing, China, in 2020. He is currently working toward the M.E. degree in electrical engineering with the College of Energy and Electrical Engineering, Hohai University, Nanjing, China.

His current research interests include the optimization of permanent magnet machines and finite element analysis.